Improved Magneto-Microfluidic Separation of Nanoparticles through Formation of the β-Cyclodextrin–Curcumin Inclusion Complex

Jordy Queiros Campos, M. Boulares, M. Raboisson-Michel, G. Verger-Dubois, J. García Fernández, G. Godeau, P. Kuzhir

Improved magneto-microfluidic separation of nanoparticles through formation of β-cyclodextrin-curcumin inclusion complex

J. Queiros Campos[1], M. Boulares[2], M. Raboisson-Michel[1,3], G. Verger-Dubois[3], J. M. García Fernández[4], G. Godeau[1] and P. Kuzhir[1*]

[1] *University Côte d'Azur, CNRS UMR 7010 Institute of Physics of Nice (INPHYNI) - Parc Valrose 06108 Nice, France*

[2] *University of Carthage, Faculty of Sciences of Bizerte, Centre des Recherches et des Technologies des Eaux (CERTE) Technopole de Borj-Cédria, Route touristique de Soliman BPn° 273 Soliman 8020 Tunisia*

[3] *Axlepios Biomedical - 1st Avenue 5th Street, 06510 Carros, France*

[4] *Instituto de Investigaciones Qumicas, CSIC and Universidad de Sevilla, Av. Amrico Vespucio 49, Isla de la Cartuja, 41092 Sevilla (Spain)*

ABSTRACT

Molecular adsorption to nanoparticle surface may switch the colloidal interactions from repulsive to attractive and promote nanoparticle agglomeration. If the nanoparticles are magnetic, their agglomerates exhibit a much stronger response to external magnetic fields than individual nanoparticles. Coupling between adsorption, agglomeration and magnetism allows a synergy between the high specific area of nanoparticles (~100 m^2/g) and their easy guidance or separation by magnetic fields. This yet poorly explored concept is believed to overcome severe restrictions for several biomedical applications of magnetic nanoparticles related to their poor magnetic remote control. In this paper, we test this concept using curcumin (CUR) binding (adsorption) to β-cyclodextrin (βCD) coated iron oxide nanoparticles (IONP). CUR adsorption is governed by host-guest hydrophobic interactions with βCD through the formation of 1:1 and, possibly, 2:1 βCD:CUR inclusion complexes on the IONP surface. 2:1 stoichiometry is supposed to promote IONP primary agglomeration, facilitating the formation of the secondary needle-like agglomerates under external magnetic fields and their magneto-microfluidic separation. The efficiency of these field-induced processes increases with CUR concentration and βCD surface density, while their relatively short timescale (< 5 min) is compatible with magnetic drug delivery application.

INTRODUCTION

For many decades, magnetic nanoparticles have attracted the attention of researchers and various manufacturers in regard to their biomedical[1-5] and environmental applications[6-9]. In many of these applications, one needs to manipulate the nanoparticles by gradient magnetic fields, as in the case of magnetic drug delivery, i.e. guiding and controlled release of a drug from nanoparticle surface to a localized treatment area[10-13]. The migration of magnetic nanoparticles along the magnetic field gradient is referred to as magnetophoresis[14] and its intensity is characterized by the magnetophoretic mobility, defined as a proportionality factor between the particle velocity and the magnetic field gradient. In other applications, one needs to separate magnetic nanoparticles from the

* Corresponding author: pavel.kuzhir@univ-cotedazur.fr

solvent capturing them on magnetized collectors. Here, we deal with magnetic separation employed in protein purification[15], immunoassays[16] and water purification[7] or pollutant detection[17]. The common point of these applications is that nanoparticles are designed to uptake the desired chemical species (proteins, antigens, pollutant molecules, etc.) which are then separated from the solvent by magnetic field gradients or concentrated on magnetized micro-collectors in order to be analyzed or removed from the system.

Magnetophoresis and magnetic separation are closely related processes that share similar challenges when applied to nanoparticles[18]. Physicochemical conditions and adsorption of molecules on the nanoparticle surface can considerably influence the magnetophoresis and magnetic separation in two opposite ways. On the one hand, the adsorption of surfactants or polymer brushes usually increases steric repulsion between magnetic nanoparticles and the distance between their metal oxide cores. This considerably weakens van der Waals attractive forces as well as magnetic dipole-dipole interactions between nanoparticles under applied magnetic fields. Such coating of nanoparticles avoids their agglomeration (both in the presence and in the absence of magnetic fields) and lowers their magnetophoretic mobility[19] and magnetic separation efficiency[20,21]. On the other hand, dispersion of magnetic nanoparticles in ionic solutions (like physiological media) or adsorption of proteins, drugs or pollutants on their surface often leads to their agglomeration because of screening of the electrostatic repulsion between them and/or appearance of attractive colloidal interactions[22-30]. This agglomeration could considerably enhance nanoparticle transport efficiency since (a) the magnetophoretic mobility of nanoparticles (or their agglomerates) is proportional to the cube of their size; (b) above some critical size and concentration, magnetic nano-agglomerates can easily form micron-sized aggregates under the applied magnetic field[31,32], which further accelerates their migration along the field gradient[19,33,34] and considerably enhances the efficiency of their magnetic separation[35].

We have recently studied this phenomenon in a particular case of adsorption of a methylene blue (MB) cationic dye on the citrate coated surface of magnetic iron oxide nanoparticles (IONP) in the context of water remediation application[30,36]. The dye absorption was found to be governed by electrostatic interactions, and the adsorbed dye formed H-aggregates (i.e. “side-by-side” aggregates) on the IONP surface. These aggregates were supposed to induce heterogeneous electric charge distribution on the IONP surface promoting attraction between nanoparticles and leading to their primary agglomeration. We have experimentally proved that such adsorption-induced primary agglomeration considerably enhances the field-induced secondary agglomeration and magnetic separation efficiency of nanoparticles as compared to the case without MB adsorption.

In the present paper, we focus on a completely different system – the uptake of curcumin (CUR) molecules by IONP and their possible agglomeration and magnetic separation, in regard of the potential biomedical applications. CUR is a strong antioxidant and a drug used for liver protection, anti-inflammatory treatment and cancer prevention - see review by Sharma et al.[37] and the references therein. The synthesis and biomedical applications of CUR-loaded IONP have been extensively studied in the literature, with

special attention to the CUR uptake and release profiles[38-44]. However, the effects of CUR adsorption on the agglomeration and magnetic separation of IONP have only been studied scarcely, despite the high relevance of these effects in magnetic drug delivery. To the best of our knowledge, only the article by Jayaprabha and Joy[45] reports on the possible agglomeration of IONP with an increasing amount of bound CUR. In that work, the IONP were coated by β-cyclodextrin (βCD) – a cage molecule with a hydrophobic cavity. Through hydrophobic interactions, the CUR molecule can enter into either one or two βCD cages, and such binding modes are referred to as 1:1 or 2:1 host-guest inclusion complexes, respectively[46]. According to Jayaprabha and Joy[45], some CUR molecules can bridge neighboring IONP, thereby leading to primary agglomerates, by forming 2:1 inclusion complexes with βCD entities at the surface of different particles, as schematically shown in Figure 1. The authors report physicochemical characterizations relevant for drug delivery and magnetic resonance imaging applications but quantification of the adsorption-induced agglomeration and magnetophoretic mobility of CUR-loaded IONP is still missing.

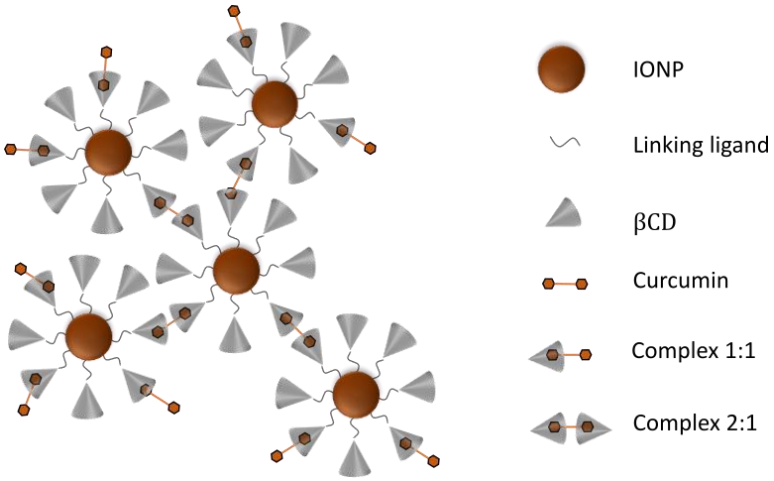

Figure 1: Possible mechanism of primary agglomeration of βCD-coated IONP through the formation of 2:1 βCD:CUR inclusion complex, as suggested by Jayaprabha and Joy[45]. The addition of CUR to the nanoparticle solution is expected to promote both 1:1 and 2:1 βCD:CUR inclusion complexes on the IONP surface

The main goal of the present study is to find experimental correlations between the amount of CUR bound to the IONP surface, the size of the nanoparticle primary agglomerates induced by the CUR uptake and the efficiency of their field-induced secondary agglomeration and magnetic separation. To this purpose, we develop a new protocol for the IONP coating process allowing the efficient incorporation of βCD units for an effective CUR uptake. Next, we study the magnetic separation of the nanoparticles in the presence of CUR using a microfluidic channel equipped with a magnetizable micropillar allowing extraction of nanoparticle agglomerates from the magnetic suspension flowing through the channel. From the general perspective, this study is oriented toward a fundamental understanding of physicochemical phenomena rather than toward the development of magnetic composite for CUR delivery. We believe that the present work will elucidate the effects of the drug binding to the IONP surface on nanoparticle agglomeration and the efficiency of their manipulation by external magnetic

fields. Moreover, the proposed method of βCD coating of the nanoparticle surface through grafting to a layer of physically adsorbed sodium polyacrylate could be useful for IONP applications in water remediation or pollutant sensing since βCD has a necessary affinity with emergent organic pollutants, as pesticides and polycyclic aromatic hydrocarbons[47-50].

EXPERIMENTAL SECTION

All chemicals were purchased from Aldrich or Merck at the highest purity grade and used without further purification. All solvents were purchased dry and were used without further distillation. 6^{I}-azido-6^{I}-deoxycyclomaltohexaose, also called β-cyclodextrin (βCD) mono-N_3 (Figure 2b) was synthesized from commercial βCD via selective tosylation of a single primary hydroxyl[51] and subsequent nucleophilic displacement of the tosylate group by azide anion[52], following previously reported protocols. The keto-enol form of curcumin (CUR) used in the present work is shown in Figure 2c.

Synthesis of IONP and functionalization by βCD

Fabrication of βCD coated IONP followed a three-step process:

1. Acid ferrofluid synthesis (suspension of bare IONP in a dilute nitric acid aqueous solution at pH~2);
2. Coupling of βCD with poly(acrylic acid) sodium salt (hereinafter denoted as PAA), 35%wt. aqueous solution, molecular weight of 15000 g/mol, via click-chemistry synthesis;
3. Coating of bare IONP by βCD/PAA polymer.

1) Magnetite (Fe_3O_4) IONP were synthesized by coprecipitation of the Fe (II) and Fe (III) ions using an ammonia solution, following Massart's method[53]. Precisely, 3.26 g of $FeCl_2$ $4H_20$ (16.4 mmol) and 8.70 g $FeCl_3$ $6H_2O$ (32.2 mmol) were dissolved in 380 ml of MilliQ water. Then, at room temperature and under magnetic stirring, 20 mL of a 25wt% aqueous ammonia solution was added to precipitate the iron salts into Fe_3O_4 IONP. The suspension was centrifuged at 11000 g. After removing the centrifuged supernatant, 40 mL of a 2 M aqueous ammonia solution was added to disperse the nanoparticles. Finally, 60 ml of 0.35 M $Fe(NO_3)$ was introduced, and the solution was left stirring for 1 h at 100 °C using mechanical agitation at 40 rpm to complete oxidation of magnetite into maghemite (γ-Fe_2O_3) IONP. These nanoparticles were washed five times with 150 mL aliquots of 1 M nitric acid and five times with deionized water before being dispersed in deionized water to obtain a pH ~2.0 solution, referenced hereinafter as "Acid ferrofluid".

2) For the covalent coupling of βCD and PAA, a highly specific methodology warranting high conversion rates (~90%) and compatible with inorganic solvent (water) was required. To reach this goal, we naturally focus on the click chemistry, namely, on the Huisgen reaction modified by Tornøe et al.[54] and Rostovtsev et al.[55]. This reaction is a regiospecific copper (I) catalyzed 1,3 dipolar cycloaddition between alkyne and azide partner to give the corresponding 1,4-disubstituted 1,2,3-triazole link. In our case, PAA polymer is initially functionalized with propargylamine, affording "Propargylamide-

polymer". The modified PAA is next engaged in the click-coupling step with βCD mono-N_3 to achieve the "βCD-polymer" where βCD is covalently linked with PAA. The main steps of the βCD-polymer synthesis are shown in Figure 2a.

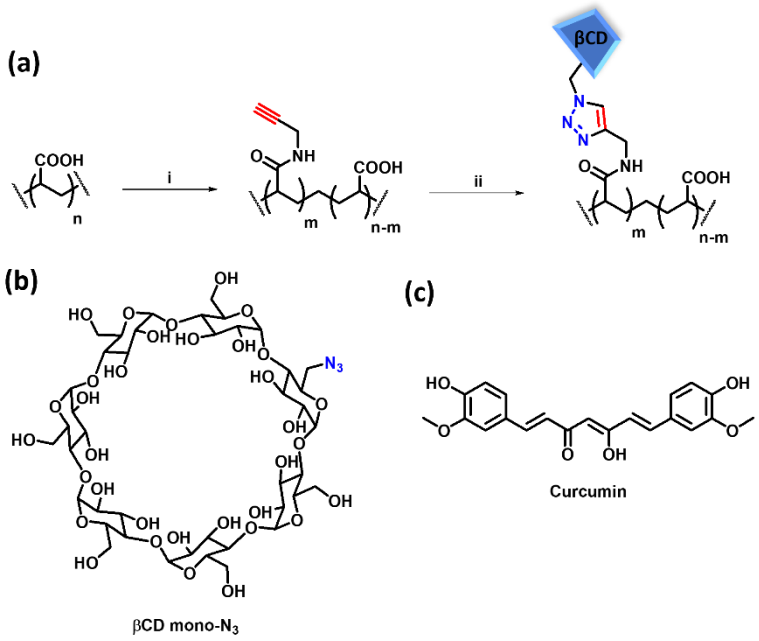

Figure 2. General scheme for polymer functionalization (a): i) Propargylamine, EDCI, DMAP and NHS, room temperature, water, 1 day. ii) βCD mono-N_3, $CuSO_4$, sodium ascorbate, 70 °C, water/ethanol (50/50), overnight. The chemical structure of βCD mono-N_3 is shown on (b). The keto-enol form of curcumin is shown in (c)

For polymer modification, we dissolved 5.71 g (1.33 mmol) of PAA in 20 ml MilliQ water. The pH was adjusted to 4.5 by the addition of hydrochloric acid. Functionalization degree is defined as the molar percentage of carboxyl groups engaged in reaction (first amidification, then click reaction with βCD mono-N_3). For example, to achieve a theoretical functionalization degree θ_{th}= 5% mol, the reactants were added in the reaction flask as follow: 5% mol dimethylaminopyridine (DMAP) (0.17g, 0.0665 mmol), 5% mol 1-Ethyl-3-(3-dimethylaminopropyl) carbodiimide (EDCI) (0.27g, 0.0665 mmol) and 5% mol N-hydroxysuccinimide (NHS) (0.16g, 0.0665 mmol) were mixed under vigorous agitation for 30 minutes at room temperature. Then, 5% mol of propargylamine was added (89 µl, 0.0665 mmol), and the solution was left under magnetic stirring for one day at room temperature. Alternatively, to achieve a functionalization degree of θ_{th}=10% mol, the same procedure was used with all chemical quantities of each reactant proportionally modified. After washing with acetone and MilliQ water, the functionalized polymer is obtained and dried under vacuum over one day to remove any trace of water. Then, βCD-polymer was assembled by reacting the Propargylamide-polymer with βCD mono-N_3. For example, in the case of θ_{th}=5% mol, 200 mg (2.7 mmol) of the corresponding Propargylamide-polymer were dissolved in 50 mL of water/ethanol (50wt/50wt) mixture. 5% mol βCD (156 mg, 1.35 mmol), 5% mol $CuSO_4$ (21mg, 1.35 mmol) and 5%mol sodium ascorbate (27mg, 1.35 mmol) were added and stirred at 70°C overnight. Finally, the mixture was dialyzed to recover the βCD polymer at the expected

maximal functionalization degree of θ_{th}=5% mol. Dialysis was performed (Dialysis tubing cellulose membrane cut off = 14000 g/mol, Sigma-Aldrich) in MilliQ water over 3 days changing the water every 4 hours. For the functionalization degree θ_{th}=10% mol, a similar protocol was respected replacing the percentage of reactants from 5% mol to 10% mol.

3) The acid ferrofluid and the final βCD polymer were mixed using an orbital shaker at 20 rpm for 1 h at room temperature and precipitated by the addition of concentrated hydrochloric acid until pH = 2. Low pH is expected to promote multi-point adsorption of the PAA/βCD polymer onto the IONP surface by carboxylate groups, while subsequent pH increase allows deprotonation of carboxylic groups and redispersion of nanoparticles that acquire negative surface charge allowing electrostatic repulsion between them, as suggested by the precipitation-redispersion mechanism[56]. The suspension was centrifuged at 11000 g to remove the excess of βCD-polymer which was not precipitated on the nanoparticles. After removing the centrifuged supernatant, an appropriate amount of MilliQ water was added, and the solution pH was adjusted to 8 with 25 % wt ammonia solution. At the end, aqueous solutions of IONP covered with a PAA/βCD layer (called hereinafter βCD ferrofluids) at two different theoretical functionalization degrees (θ_{th}=5% mol or θ_{th}=10% mol) were obtained.

Physicochemical characterization

The weight concentration of the PAA/βCD polymers in the stock concentrated solutions after dialysis was determined by the dry residue method. Iron concentration in the IONP suspensions was measured by an inductive coupled plasma atomic emission spectrometer (ICP-AES, Perkin Elmer Optima 8000 DV). Before making these measurements, samples containing the nanoparticles were dissolved in concentrated hydrochloric acid (10 mol/L) until the total dissolution of Fe(III) and Fe(II) ions. The measured iron molar concentration C_{Fe} was then converted to weight concentration c_w (g/L) and volume fraction φ of IONP using the following expressions: $c_w = C_{Fe}\, M_{w,Fe2O3}/2$ and $\varphi = c_w/\rho_{Fe_2O_3}$, where $M_{w,Fe_2O_3} = 160\,\mathrm{g/mol}$ and $\rho_{Fe_2O_3} \approx 5\,\mathrm{g/cm^3}$ are the maghemite molar mass and density, respectively. Transmission electron microscopy (TEM) of dried dilute aqueous solutions of bare and βCD-coated IONP was carried out on a JEOL 1400 microscope operated at 100 kV acceleration voltage. The magnetization curves of the bare IONP and βCD-coated IONP were measured at room temperature using a vibrating sample magnetometer (VSM 4500 EG&G Princeton Applied Research, US). To this purpose, the ferrofluid samples were dried overnight in an oven at 100 °C, and the mass fraction φ_w of remaining iron oxide was determined by weighing the samples before and after drying. With the knowledge of φ_w and $\rho_{Fe_2O_3}$ values and assuming a log-normal distribution of nanoparticle volumes with a dimensionless width σ, the saturation magnetization M_S and the volume-weighted average diameter $d_{M,V}$ of IONP metal oxide cores were subsequently determined using a standard procedure[57,58]. The number-weighted average diameter was then evaluated as $d_{M,N} = d_{M,V}\exp(-\sigma^2/3)$. The hydrodynamic size distribution of the bare and coated IONP was measured by dynamic light scattering (DLS) using a zeta sizer Nano ZS (Malvern Instruments, UK) operating at a 173° scattering angle. The electrophoretic mobility of IONP and the electric conductivity of IONP solutions were measured by the

same DLS apparatus. Prior to the DLS/electrokinetic measurements, parent acid and βCD ferrofluids were diluted in MilliQ water to c_w=0.184 g/L, with attention to possible changes in pH and conductivity. Based on the electrokinetic model of porous agglomerates[59], the electrophoretic mobility was converted to the particle zeta potential and surface density of the effective charge, $|Z_{eff}|$ (in number of elementary charges per nm^2), using the expressions developed in Supporting Information of Talbot et al.[30]. The electric conductivity allowed evaluation of the ionic strength of the samples and, subsequently, the Debye screening length κ^{-1} using expressions developed by Ezzaier[60].

The amounts of βCD polymer bound to the IONP surface were estimated from thermogravimetric analysis (TGA) performed on a Netzsch Jupiter ECO TGA STA449F5 apparatus. The samples were heated from 40 °C to 800 °C with a heating rate of 10 °C/min under a nitrogen stream of 50 mL/min, the temperature was then stabilized at 800 °C for 1 h. The βCD functionalization degree θ and the weight ratio of the βCD mass to the mass of the whole βCD polymer, $X_{\beta CD}$, were determined using conductimetric titration on Nano ZS zeta-sizer using curcumin (CUR) molecule as a probe following the general analytical protocols of inclusion chemistry[46,61] - cf. Figure S4 with detailed explanation in SI, Section A. The obtained values θ were compared to the theoretical values θ_{th}. On the other hand, molar ratio θ_{pr} of the grafted propargylamine to the whole propargylamide polymer was assessed through nuclear magnetic resonance (NMR) ^{1}H measurements performed on a Bruker 400 MHz apparatus, using CF_3COOD as a solvent. NMR spectra show chemical shifts in ppm, while the ratio of areas below the relevant peaks allows evaluation of θ_{pr}. The ratio $E = \theta/\theta_{pr}$ was then calculated considered as an experimental value of the βCD grafting efficiency using the click chemistry.

CUR binding to βCD-coated IONP and primary (adsorption-induced) agglomeration

First, since CUR is insoluble in pure water, we prepared CUR stock solution in pure ethanol at CUR molar concentration of 10^{-2} M. Then, we mixed the CUR/ethanol stock solution with βCD ferrofluids. By adding an appropriate amount of MilliQ water and pure ethanol, we realized mixtures (denoted as βCD-FF-CUR samples) at a fixed weight ratio of ethanol/(water+ethanol), w=0.3, at the desired IONP weight concentration c_w=1 or 8 g/L, at different CUR molar concentrations $C_{CUR,0}$ and two different βCD functionalization degrees θ. The ratio w=0.3 ensured a good CUR solubility in the samples at the highest concentrations $C_{CUR,0}$=1.2 mM, as checked against the CUR solubility limit in ethanol/water solvent[62] at 25°C. The βCD-FF-CUR samples were prepared using the following sequence: first, parent samples of βCD ferrofluids were mixed with appropriate amounts of water and ethanol; then, an appropriate amount of the stock CUR/ethanol solution was added followed by stirring using a rotary shaker at 20 rpm for 20 min.

Most standard analytical technics appeared to be inappropriate for the study of CUR binding to IONP for either the abundance of iron signal (UV-visible spectrophotometry, NMR) and/or impossibility to efficiently separate the supernatant from βCD-FF-CUR samples using Macrosep Advance centrifugal filters (VWR, France) reacting with CUR and affecting its dosage. These experimental constraints also hinder

the evaluation of the stoichiometry of βCD:CUR inclusion complexes in the presence of IONP. Thus, the kinetics of the CUR binding to βCD-coated IONP and binding equilibrium was assessed by fluorescence experiments conducted on the samples containing nanoparticles. To this purpose, we placed βCD-FF-CUR samples in a Clariostar Plus fluorescence plate reader from BMG Labtech. Each sample was excited with a wavelength of 430 nm for 3 μs and the induced fluorescence intensity was measured synchronously with illumination at the wavelength of 590 nm. The samples were inserted into the plate reader at different times t elapsed from the sample preparation (end of the shaking) ranging from 0 to 12h. This allowed observing the evolution of the fluorescence intensity, $F(t)$ with time t and relating it to the molar concentration C_{CUR} of free (unbound) CUR and the surface density n_{CUR} (in nm^{-2}) of CUR bound to IONP surface as a function of time, as detailed in SI, Section B. The C_{CUR} and n_{CUR} values corresponding to the plateau of the $F(t)$ curve were considered as equilibrium values allowing us to plot an adsorption isotherm $n_{CUR}=f(C_{CUR})$.

Additionally, the kinetics of the CUR binding was correlated to the kinetics of IONP agglomeration measured by DLS (Subsection "Physicochemical characterization"). Briefly, diluted samples (at IONP weight fraction c_w=0.184 g/L, two CUR molar concentrations, $C_{CUR,0}$=0.534 mM and 0.934 mM and two functionalization degrees θ) were introduced at different elapsed times t to the zeta-sizer apparatus and the average hydrodynamic diameter d_H was plotted as a function of t. At the same time, the DLS measurements were conducted at a fixed elapsed time t=12 h (when the equilibrium final size was established) as a function of the CUR concentration. Experimental dependencies $d_H(C_{CUR})$ were finally correlated with the experimental adsorption isotherms $n_{CUR}(C_{CUR})$.

Secondary (field-induced) agglomeration and magnetic separation of IONP

In these experiments, we used βCD-FF-CUR liquid samples prepared as described in Subsection "CUR binding to βCD-coated IONP and primary (adsorption-induced) agglomeration" at a desired CUR molar concentration $0 \leq C_{CUR,0} \leq 0.934$ mM, two different β-CD functionalization degrees and fixed IONP weight concentration c_w=8 g/L, corresponding to nanoparticle volume fraction φ=0.16%vol.

Polydimethylsiloxane (PDMS) microfluidic channels used for the secondary agglomeration (Figure 3a) and magnetic separation (Figure 3b) experiments were manufactured by a soft photolithography method, as described in Ezzaier et al.[21]. Channels were made 50 μm in height, 1 mm in width and 15 mm in length. The channel used for magnetic separation was equipped with a PDMS cylindrical micro-pillar, 50 μm in diameter and 50 μm in height, filled with magnetizable carbonyl iron microbeads (HQ grade BASF, Germany). The microbeads had an average diameter of 1-3 μm, a saturation magnetization of 1.36×10^6 A/m. Negligible remnant magnetization of the microbeads allows considering the magnetizable micropillar as a magnetically "soft" body with the relative magnetic permeability evaluated to be $\mu\approx4$ in our experimental magnetic field range. The micropillar was situated perpendicular to the channel lower and upper walls and spanned all the height of the channel. Thin, flexible polyvinyl chloride (PVC) tubes

(internal/external diameter of 0.5/1 mm) were introduced to ensure the entry and exit of the solution into the channel at both ends. In both experiments, the channels were filled with βCD-FF-CUR liquid samples.

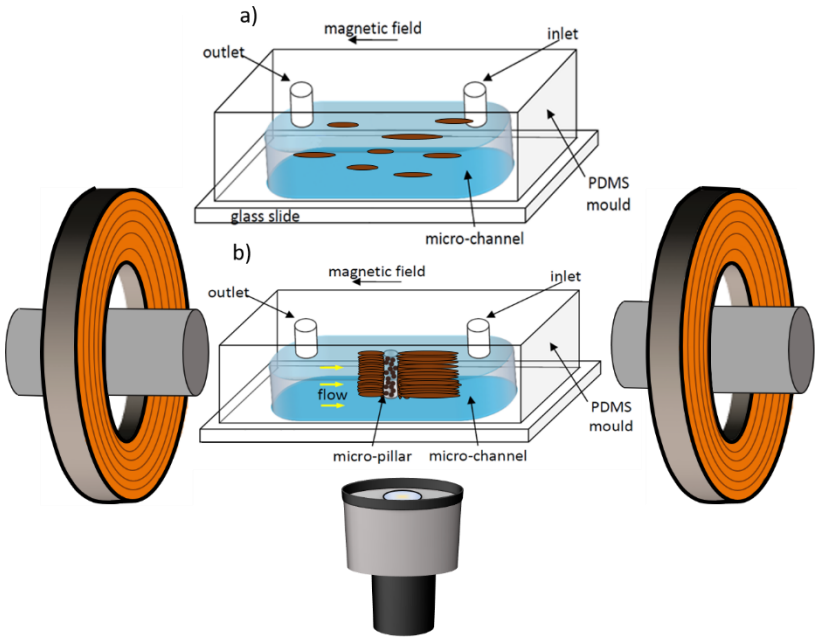

Figure 3. Sketch of the experimental setup with two types of microfluidic channels (represented in enlarged scale): without micropillar used for the field-induced agglomeration when needle-like aggregates are visualized (a), and with a micropillar used for the magnetic separation when the field-induced aggregates accumulate around the magnetized micropillar and are separated from the suspending liquid under flow (b).

During experiments on field-induced nanoparticle agglomeration, the suspension was injected into the microfluidic channel using a syringe. The channel was placed on a table of an optical transmission microscope (Nikon Daphot, Japan). A homogeneous permanent magnetic field of intensity H=13.5 kA/m was established using a pair of Helmholtz coils placed on both sides of the microscope, as shown in Figure 3. Once the magnetic field was applied, the primary nanoparticle agglomerates (formed in the absence of field) began to interact strongly with each other and formed elongated micron-sized aggregates aligned with the magnetic field. We acquired the images every 0.5 seconds for a total duration of 15 min. A x4 plan Nachet France magnification objective and a complementary metal-oxide semiconductor (CMOS) Color Camera (PixelLink PL-D755CU-T 5MP, Canada) placed under the microscope table were used. The image sequence was then processed using the ImageJ software, which calculated the length distribution and the average length of the field-induced aggregates as a function of time (see SI, Section C and Figure S10 for details).

For magnetic separation experiments, the entrance to the channel (Figure 3b) was connected to a syringe pump (PHD Ultra Harvard Apparatus, USA) delivering nanoparticle suspension at a constant flow rate. The desired flow rate was situated in the range $1 \leq Q \leq 5$ µl/min. The average suspension speed through the channel was evaluated as $u = Q/A$, with A= 5×10^{-8} m^2 being the cross-section of the channel. A few minutes after the flow was induced, a magnetic field of intensity H=13.5 kA/m was applied parallel to

the flow direction. The magnetized micropillar created a strong magnetic field gradient around itself and captured the nanoparticle primary agglomerates. They accumulated around the micropillar and formed anisotropic deposits on the micropillar lateral surface, as schematically shown in Figure 3b. The process of accumulation of the primary agglomerates around the micropillar was recorded every 0.5 s for 15 min. The images were then processed using the ImageJ software, which enabled the measurement of the horizontal projected area $S(t)$ of the deposits (hereinafter called the deposit area) at each moment of time t (see SI, Section C and Figure S11 for details). The relative surface of the deposits was introduced as follows: $s(t) = (S(t) - S_0)/S_0$, where S_0 is the micropillar cross-section. Thus, the dependence $s(t)$ quantified magnetic separation efficiency as a function of the CUR concentration $C_{CUR,0}$ and the βCD functionalization degree θ.

All experiments were performed three times, and all physical values represent an average of the three measurements. The error bars represent the standard deviation of the values obtained from the three measurements.

RESULTS AND DISCUSSION

Characterization of bare and βCD coated IONP and their solutions

The weight concentration and volume fraction of IONP in the parent βCD ferrofluid are c_w=9.92 g/L and φ=0.20%, as determined by ICP-AES. TEM images of bare and βCD-coated IONP are shown in Figure S1 in Supporting Information (SI). The βCD polymer layer on the particle surface is not visible in TEM images because of the low optical contrast (with respect to the electron beam) of the polymer and insufficient spatial resolution. The metal oxide cores of bare and coated IONP have the same shape and same average diameter of d≈10 nm, so that polymer coating realized after nanoparticle synthesis does not change the particle morphology and size. Magnetization curves on acid and βCD ferrofluids (Figure S2) allowed determining the saturation magnetization of metal oxide cores of IONP, M_S, along with their metal oxide core volume-weighted average diameter, $d_{M,V}$. Values of $M_S = 310 \pm 5$ kA/m (corresponding to 62±1 emu/g) and $d_{M,V}$=11±1 nm are obtained for both bare and coated IONP. The number-weighted average diameter $d_{M,N}$ was found to be slightly smaller than $d_{M,V}$, but the difference enters the confidence interval (±1 nm) of the magnetization curve fit. The M_S value is somewhat lower than the bulk maghemite saturation magnetization (~380 kA/m or ~76 emu/g) likely because of spin canting effect[63], while $d_{M,N} \approx d_{M,V}$ value agrees with the average TEM size d≈10 nm.

The weight ratio of the βCD polymer mass to the IONP metal oxide core mass is X_p=0.42±0.10 g/g, as assessed through TGA (Figure S3 with analysis in SI, Section A). On the other hand, the molar ratio (functionalization degree) and the weight ratio of the βCD to the whole βCD/PAA polymer are θ=3.4±0.2% mol, $X_{\beta CD}$=0.34±0.02 g/g for the theoretical functionalization degree θ_{th}=5% mol and θ=4.7±0.3% mol, $X_{\beta CD}$=0.43±0.03 g/g for θ_{th}=10% mol, as evaluated through conductivity measurements (Figure S4 and analysis in SI, Section A). At the same time, the NMR spectra (Figure S5 and analysis in SI, Section A) give us access

to the functionalization degree θ_{pr} of the propargylamine that serves as a linker between the PAA chain and βCD molecules. We find θ_{pr}=3.3±0.5% mol at θ_{th}=5% mol and θ_{pr}=6.5±0.8% mol at θ_{th}=10% mol. Thus, the efficiency of the βCD grafting to the propargylamine modified PAA is characterized by the magnitude $E=\theta/\theta_{pr}\times 100$ (in %) equal to E~84-100% for θ_{th}=5% mol and E~60-88% for θ_{th}=10% mol that is within an expected range for the click chemistry yield. The product of X_p and $X_{\beta CD}$ values gives us the weight ratio of the mass of βCD molecules present on the IONP surface to the mass of the IONP metal oxide cores $X=X_pX_{\beta CD}$=0.14±0.01 g/g and 0.18±0.01 g/g for the two functionalization degrees. We can also evaluate the surface density of the βCD molecules on the IONP surface as $n_{\beta CD} = X\,N_A/\left(M_{w,\beta CD}S\right) = 0.62 \pm 0.06\ \mathrm{nm}^{-2}$ and $0.77 \pm 0.08\ \mathrm{nm}^{-2}$ for the two functionalization degrees, with $N_A \approx 6\times 10^{23}\ \mathrm{mol}^{-1}$ being the Avogadro number and $S = 6/(\rho_{Fe2O3}d) \approx 120\ \mathrm{m}^2/g$ – the specific area of metal oxide cores of IONP of a TEM diameter d=10 nm. All these material balance quantities are summarized in Table 1.

Table 1. Characterization of amounts of βCD-polymer on IONP surface

Theoretical functionalization degree θ_{th} (% mol)	5	10
Experimental functionalization degree θ (% mol)	3.4±0.2	4.7±0.3
efficiency of the βCD grafting E (%)	84-100	60-88
Weight ratio whole polymer/IONP X_p (g/g)	0.42±0.10	0.42±0.10
Weight ratio βCD/whole polymer $X_{\beta CD}$ (g/g)	0.34±0.02	0.43±0.03
Weight ratio βCD/IONP X (g/g)	0.14±0.01	0.18±0.01
Surface density of grafted βCD $n_{\beta CD}$ (nm^{-2})	0.62±0.06	0.77±0.08

Physicochemical characteristics of the nanoparticle solutions are summarized in Table S1. Colloidal stability of bare IONP in the dilute solution of nitric acid (at pH~2 in parent acid ferrofluid at c_w=9.92 g/L) is ensured by electrostatic repulsion between positively charged nanoparticles. When diluted to c_w=0.184 g/L (concentration compatible with electrokinetic and DLS measurements), the solution pH rises to ~3, zeta potential is ~+30 mV, the surface density of the effective charge $|Z_{eff}|$~0.03 nm^{-2} and the average hydrodynamic size is d_H~54 nm pointing out to some agglomeration of IONP even though this dilute solution remains stable for a few months.

When adding βCD polymer following the precipitation/redispersion protocol (Subsection "Synthesis of IONP and functionalization by βCD" of the Experimental Section), the polymer is expected to adsorb onto the IONP surface by some of its

carboxylic groups and adopt a "loop and train" surface conformation[64], as reported for PAA adsorption onto iron oxide surface[65,66]. Free unbound carboxylate groups situated on the "loops" are mostly deprotonated at nearly neutral pH~7 and contribute to the negative electric charge of the IONP surface (zeta potential ~–30 mV, the surface density of the effective charge $|Z_{eff}|$~0.03 nm^{-2}, cf. Table S1), thus ensuring electro-steric repulsion between nanoparticles, as reported by Marins et al.[67] and schematically shown on Figure S6. However, the IONP hydrodynamic size d_H~64 nm indicates some agglomeration occurring likely because of bridging of a few neighboring nanoparticles by relatively long PAA chains ($M_{w,PAA}$=15 kg/mol) adsorbed to the surfaces of at least two neighboring particles. The hydrodynamic size distribution with respect to the scattered light intensity (intensity distribution) of bare IONP dispersed in nitric acid solution and of βCD-coated IONP diluted in MilliQ water are shown in Figure 4a by black solid and black dashed curves, respectively. In both cases, the size distribution is relatively broad and corresponds to relatively large polydispersity index (PDI) values, listed in Table S1.

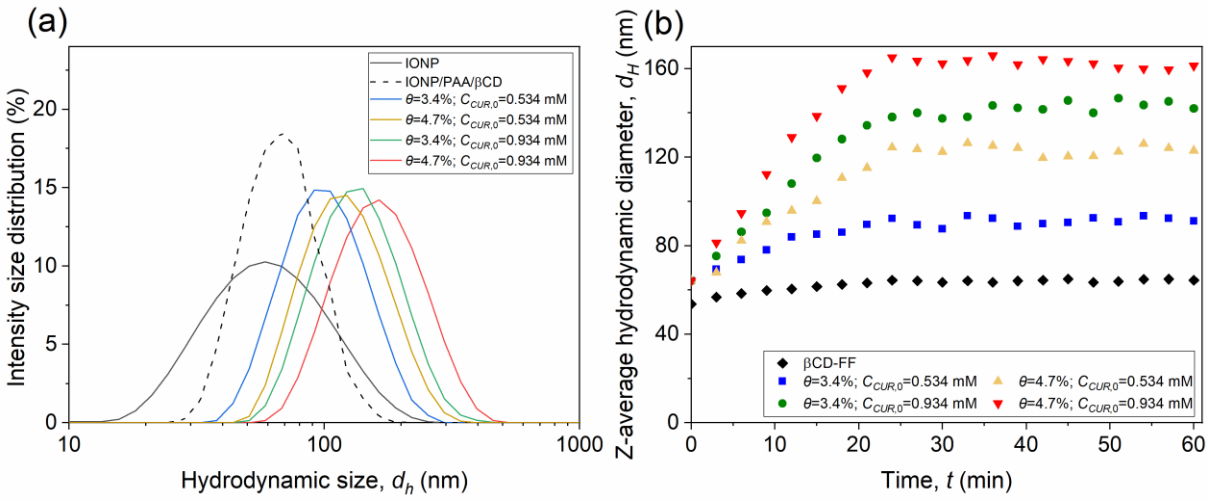

Figure 4. Intensity size distribution of IONP primary agglomerates measured by DLS at IONP weight concentration c_w=0.184 g/L (a). The colored curves present the data for βCD-FF-CUR samples at two different CUR molar concentrations $C_{CUR,0}$ and two different functionalization degrees θ. Average hydrodynamic size as a function of time (elapsed from the end of the sample shaking) for the samples of two different $C_{CUR,0}$ and θ values (b).

Primary agglomeration by CUR addition

The addition of CUR/ethanol solutions to the βCD ferrofluids induces a stronger IONP agglomeration as compared with that observed for pure βCD ferrofluids, as revealed by a progressive shift of the hydrodynamic size distribution to higher size values with increasing CUR molar concentration $C_{CUR,0}$ and the functionalization degree θ (Figure 4a). The Z-average diameter increases from d_H=64 nm in absence of CUR to 161 nm for $C_{CUR,0}$=0.934 mM and θ=4.7% mol, as indicated in Table S1. The results presented in Figure 4a and Table S1 were collected at the elapsed time t=12 h after the mixture between βCD ferrofluid and CUR solution. Kinetics of IONP agglomeration upon CUR addition was followed by DLS and is reflected in Figure 4b, where the average

hydrodynamic size is plotted as a function of time (elapsed from the end of the sample shaking) for the samples of two different $C_{CUR,0}$ and θ values. As is seen from this figure, the agglomerate size increases on the timescale of 20 min and achieves a plateau.

As it follows from electrokinetic measurements on dilute βCD-FF-CUR (c_w=0.184 g/L) mixtures, CUR addition does not change significantly neither the surface effective charge density of IONP nor the Debye screening length at the considered solution pH~7. This is consistent with the overall zero charge of the protonated CUR molecule at this pH since the lowest pK_a value in aqueous solutions[68,69] ranges from 7.75 and 8.89. We can therefore suppose that electrostatic interactions remain unaltered by CUR addition and the nanoparticle agglomeration should arise from non-electrostatic ones. As mentioned in Introduction section, the formation of the 2:1 βCD:CUR host-guest inclusion complex bridging two neighboring nanoparticles (Figure 1) could be at the origin of IONP primary agglomeration in the presence of CUR. We next tried to characterize interactions between dissolved CUR molecules and βCD cages fixed at the IONP surface, taking into account that immobilization of βCD on the IONP surface could displace the complexation equilibrium between βCD and CUR, as compared to the case with dissolved βCD. It is known that dissolved βCD forms mainly a 1:1 inclusion complex with CUR[70]. By conductivity measurements, we have also checked that our βCD polymer aqueous solution mixed with CUR/ethanol solution develops only a 1:1 inclusion complex (Figure S4 and explanation in SI, Section A).

The interaction between CUR and βCD polymer immobilized on IONP surface was analyzed through fluorescence intensity measurements following the protocol established in Subsection "CUR binding to βCD-coated IONP and primary (adsorption-induced) agglomeration" of the Experimental Section. A detailed analysis of the fluorescence data along with the method of calculation of the surface density of bound CUR n_{CUR} is presented in SI (Section B, Figure S7).

The evolution of the bound CUR, n_{CUR}, with time (elapsed from the end of the sample shaking) is shown in Figure 5a for IONP weight concentration c_w=8g/L, three different molar concentrations $C_{CUR,,0}$ of total CUR and two βCD functionalization degrees θ. This graph shows an increase of the bound CUR at a timescale of about 30 min followed by a plateau. The CUR binding timescale compares well with the IONP agglomeration timescale (~20min) established previously by DLS measurements (Figure 4b). Two matching timescales indicate that the CUR uptake onto the IONP surface and IONP agglomeration are very likely interconnected processes.

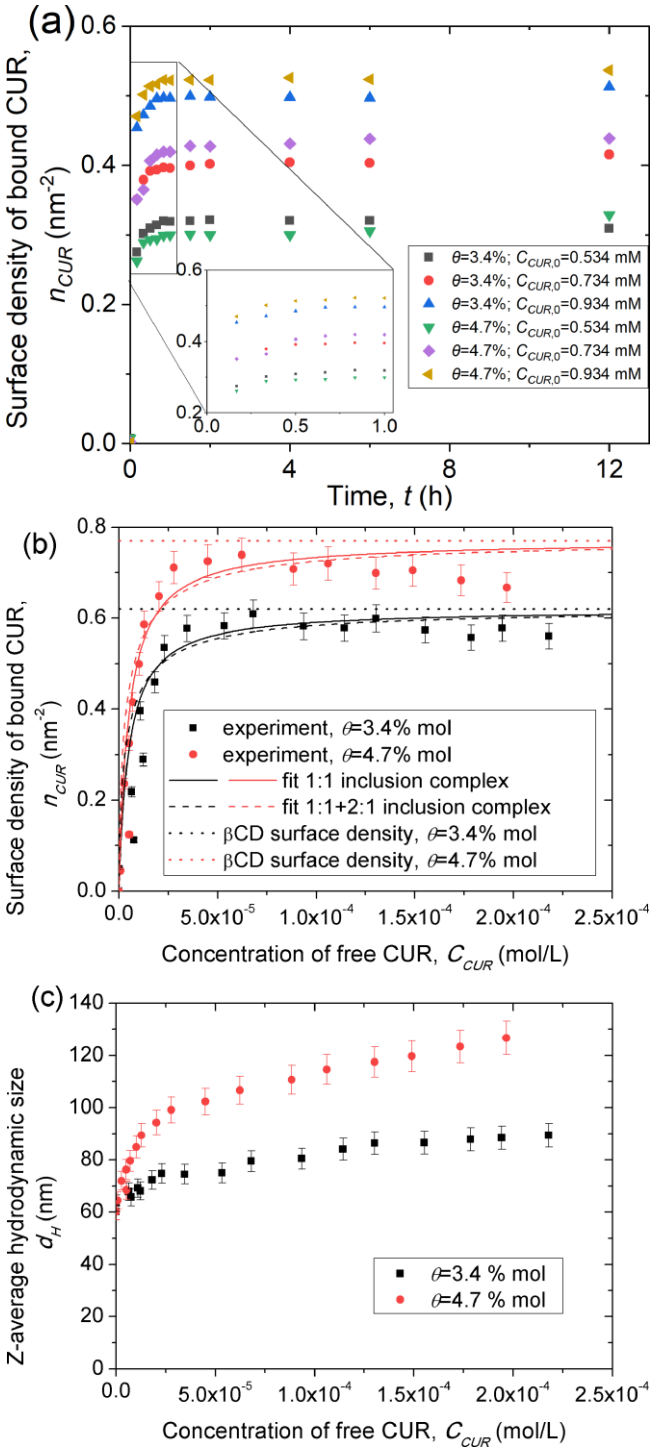

Figure 5. Kinetics of the CUR binding to the βCD-coated IONP (a). Adsorption isotherm of CUR at βCD-coated IONP (b). Average hydrodynamic size of primary agglomerates as function of the free CUR concentration (c). The inset in (a) shows an enlarged view in the time interval of 0 – 1h. The solid lines in (b) stand for the fit by Langmuir adsorption model [Eq. (2)] allowing for a single stoichiometry with the 1:1 inclusion complex (K_1=2×10^5 L/mol); the dashed lines stand for the fit by the complexation model [Eq. (1)] allowing for coexistence of 1:1 and 2:1 inclusion complexes (K_1=3×10^5 L/mol, K_2=1)

The plateau value of n_{CUR} in Figure 5a allows plotting the adsorption isotherms of CUR in terms of the steady-state value of the surface density n_{CUR} as a function of the molar concentration C_{CUR} of free CUR remaining in the solution. These isotherms are presented in Figure 5b for both functionalization degrees θ=3.4 % mol and 4.7% mol and for the

IONP weight concentration c_w=1 g/L. Notice that for the highest IONP concentration c_w= 8 g/L, we could not realize reliable measurements at high CUR concentrations because of the CUR solubility limit in the water-ethanol mixture. Both isotherms show a substantial increase in the surface density of bound CUR with increasing concentration of free CUR. The isotherm at θ=4.7% mol shows a slight peak followed by a slight gradual decrease. The same behavior seems to be observed at θ=3.4%, however, the decrease of the isotherm at high values of C_{CUR} is hardly discernable from error bars. For both functionalization degrees, the maximal values of the surface density of bound CUR, n_{max}, approach (within the analytical errors) the surface density of βCD available on the IONP surface, i.e. $n_{\beta CD}$≈0.62 nm^{-2} and 0.77 nm^{-2} at θ=3.4% mol and 4.7% mol, respectively. This indicates that small CUR molecules can likely penetrate the porous primary agglomerates and bind most of the available β-CD not only on the agglomerate surface but also in its interior. Furthermore, approximate equality, $n_{max} \approx n_{\beta CD}$, clearly proves that CUR adsorption is dominated by host-guest hydrophobic interaction with βCD, while interactions between CUR and acrylate moieties of the βCD-polymer or with iron oxide surface are likely negligible, as expected for the protonated form of CUR at neutral pH[69]. On the other hand, by DLS measurements, we have found a monotonic increase of the hydrodynamic size of primary agglomerates with the concentration of free CUR, as shown in Figure 5c. This increase is linear when plotted against the total molar concentration $C_{CUR,0}$ of added CUR [Figure S8]. Thus, a slight decrease of the surface density of bound CUR after reaching the adsorption maximum can likely be ascribed to two following effects. At first glance, a number of available βCD adsorption sites inside the primary agglomerates could decrease as their size increases with C_{CUR}. Secondly, the increasing size of the primary agglomerates could require an increasing amount of 2:1 βCD:CUR inclusion complexes binding neighboring nanoparticles (cf. Figure 1), as the ratio of contact points between nanoparticles to the whole number of particles per agglomerate increases with the size of the latter. If the number of 2:1 inclusion complexes increases with C_{CUR}, the surface density of bound CUR should decrease. When the surface density of bound CUR is normalized by the surface density n_{max} of available βCD, the adsorption isotherms $n_{CUR}/n_{max} = f(C_{CUR})$ collapse onto a single curve for two functionalization degrees θ - see Figure S9a. This was expected since, at a first approximation, the adsorption equilibrium should not depend on the amount of available βCD.

Finally, we have tried to establish a simple adsorption model based on the complexation equilibrium between CUR and βCD immobilized onto the IONP surface. The model accounts for the possible coexistence of 1:1 and 2:1 inclusion complexes with associated complexation constants equal to $K_1 = n_1/(n_0 C_{CUR})$ and $K_2 = n_2\, n_{max}/(n_0 n_1)$, with n_1, n_2 being surface densities (in nm^{-2}), of 1:1 and 2:1 inclusion complexes formed on IONP surface; n_0 – the surface density of the unoccupied βCD sites (not bound to CUR) and n_{max} – the total surface density of βCD equal to maximal possible adsorption density of CUR. Along with material balance, the model gives the following expressions for the adsorption isotherm:

$$\frac{n_{CUR}}{n_{max}} = \frac{n_1+n_2}{n_{max}} = \left[K_1 \frac{n_0}{n_{max}} + K_1K_2 \left(\frac{n_0}{n_{max}}\right)^2\right] C_{CUR}, \quad (1a)$$

$$\frac{n_0}{n_{max}} = \frac{-(K_1C_{CUR}+1)+\sqrt{(K_1C_{CUR}+1)^2+8K_1K_2C_{CUR}}}{4K_1K_2C_{CUR}}, \quad (1b)$$

which reduce to the Langmuir adsorption equation[71] for the case of the 1:1 inclusion complex only:

$$\frac{n_{CUR}}{n_{max}} = \frac{n_1}{n_{max}} = \frac{K_1C_{CUR}}{1+K_1C_{CUR}} \text{ at } K_2 = 0. \quad (2)$$

The experimental adsorption isotherms in Figure 5b were fitted to these both equations, with the complexation constants K_1 and K_2 being adjustable parameters and n_{max} value fixed to that of the βCD surface density (0.62 nm^{-2} and 0.77 nm^{-2} for θ=3.4 % mol and 4.7% mol, respectively). The difference between predictions of these equations is minimal (solid lines for Eq. (2) and dashed lines for Eq. (1) in Figure 5b) indicating that it is unfortunately impossible to distinguish between the cases of solely 1:1 inclusion complex and coexisting 1:1 and 2:1 complexes. The data and both fits collapse onto a single line in linear Langmuir plots [Figure S9b] with no visible deviation from linear behavior that would be expected from the mathematical structure of Eq. (1). Furthermore, the model does not account for a possible increase of the number of adsorption sites for 2:1 complexes with increasing agglomerate size and therefore predicts a monotonic increase of the adsorption isotherm for any inclusion complex stoichiometry, in some disagreement with experiments. According to the considered complexation equilibrium, the ratio of the 2:1 to 1:1 complexes, $n_2/n_1 = K_2\, n_0/n_{max}$ gradually decreases with increasing free CUR concentration C_{CUR} and vanishes at $K_1C_{CUR} \gg 1$, as shown in Figure S9c. Thus, the model predicts only 1:1 complexes at the adsorption plateau with the surface density of bound CUR approaching the surface density n_{max} of available βCD, or $n_{CUR}/n_{max} \to 1$, as shown in Figure S9a. As already mentioned, this prediction is likely not appropriate for the present system with the availability of the 2 βCD complexation sites situated on neighboring nanoparticles increasing with the agglomerate size.

In summary, the ensemble of fluorescence and DLS measurements (Figures 4 and 5) does not allow explicit proof for the IONP primary agglomeration through the formation of 2:1 βCD:CUR inclusion complexes. However, these results clearly indicate an interplay between the CUR binding to IONP and their primary agglomeration through the similar kinetics and some similarity of the equilibrium states: higher CUR concentration implies larger aggregates, and this is likely at the origin of a slight decrease of the amount of bound CUR. Both processes are expected to be governed by the minimum energy principle, through an optimal combination of the agglomerate size (affecting the surface and interparticle interaction energies), the amount of bound CUR and the stoichiometry of the CUR:βCD inclusion complexes (implying entropy changes and adsorption energies). The adsorption model has to be reformulated on a statistical mechanics basis to give a realistic picture of CUR binding and capture possible non-monotonic shapes of the isotherms.

Secondary (field-induced) agglomeration

For secondary (field-induced) agglomeration experiments, βCD-FF-CUR mixtures were prepared as indicated in Subsection "CUR binding to βCD-coated IONP and primary (adsorption-induced) agglomeration" of the Experimental Section at IONP weight concentration c_w=8 g/L, two different CUR molar concentrations $C_{CUR,0}$ and two different βCD functionalization degrees θ. 1 h after preparation (the time sufficient to achieve a steady size of the primary agglomerates – cf. Figure 4b), the suspension was injected to the microfluidic channel and a magnetic field of an intensity H=13.5 kA/m was applied, as detailed in Subsection "Secondary (field-induced) agglomeration and magnetic separation of IONP" of the Experimental Section.

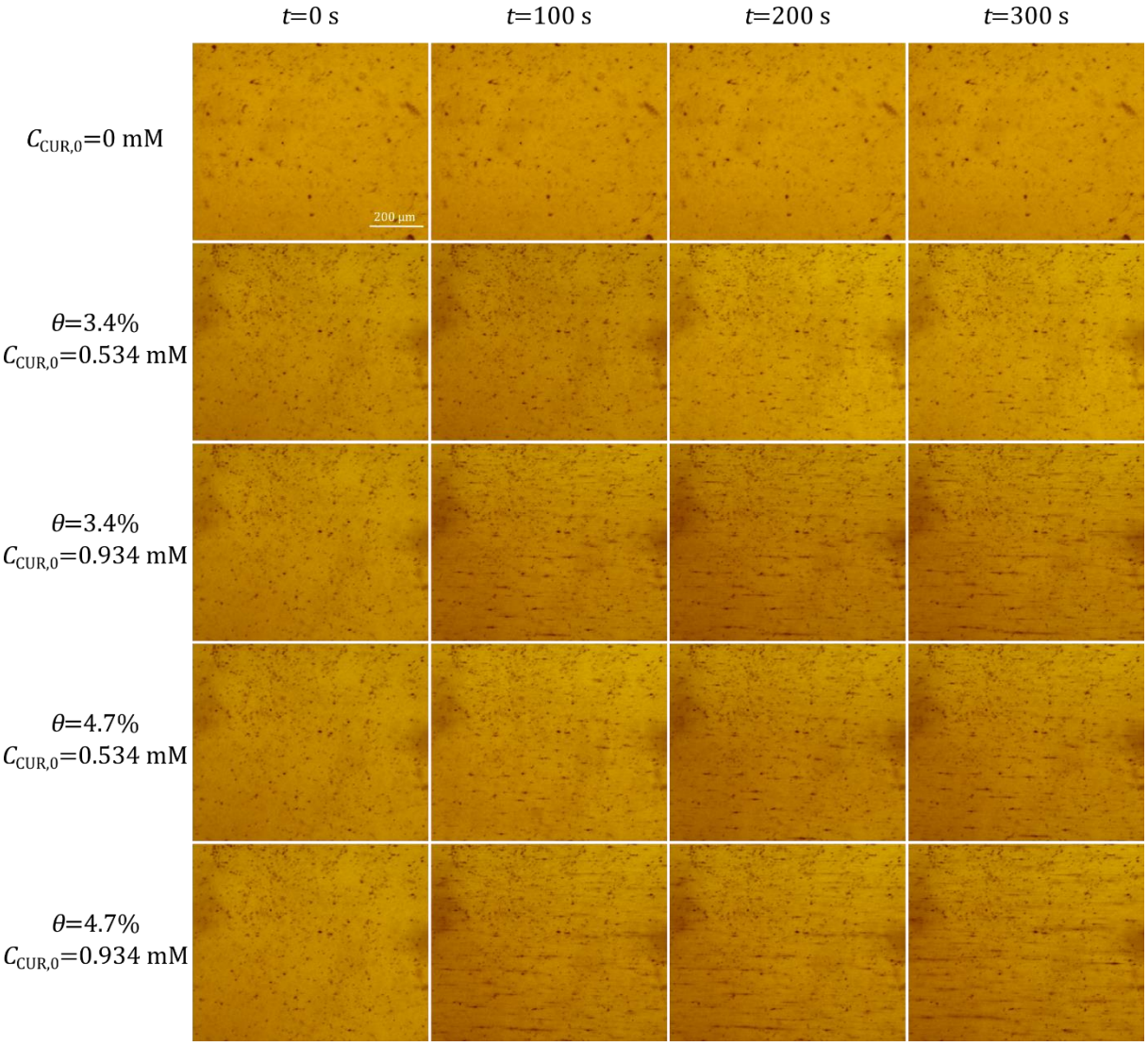

Figure 6. Snapshots of samples showing the secondary agglomeration induced by the magnetic field at H=13.5 kA/m and the times (elapsed from the switching on the magnetic field) t=0, 100, 200 and 300 s. In the absence of curcumin (first row), the sample macroscopic aspect remained the same before, during and after the application of the magnetic field, which led us to assume the absence of field-induced agglomeration at $C_{CUR,0}$=0.

Immediately after magnetic field application, micron-sized needle-like aggregates composed of a large number of primary agglomerates were formed and grew over time along the magnetic field direction, as shown in snapshots of Figure 6. The full resolution version of this figure is available as a separate .tiff file in SI.

The static micron-sized artefacts observed in the snapshots correspond to dust particles that entered the microfluidic channel. Washing the channel does not allow complete removal of these particles. However, we have never observed any effect of these particles on the formation of field-induced agglomerates. Significantly, in the absence of CUR, no distinguishable field-induced agglomeration is observed (1st row in Figure 6). For all other samples containing CUR, the field-induced agglomeration is evident, and the size of the secondary agglomerates gradually increases with time before reaching a steady-state value at $t > 300$ s. Noteworthy, coalescence of neighboring aggregates is not observed, implying that their growth corresponds to diffusion and magnetophoresis of the primary agglomerates towards the secondary ones, as shown in detail in our previous study[31]. Third, when the magnetic field was switched off, the secondary agglomerates did not disappear. This could be another sign of the bridging of IONP by CUR through the formation of 2:1 inclusion complexes with β-CD on the IONP surface. Such a situation recalls magnetic field-enhanced agglutination immunoassays, in which the applied magnetic field induces an irreversible agglomeration of antibody-coated magnetic beads through binding them by antigens present in the solution[16,72]. It could be anticipated that in practical drug delivery application, CUR loaded IONP will spontaneously release CUR from the βCD cavities into the medium free from CUR once delivered to the target tissue, as suggested in a review by Stella et al.[73]. It is thus possible that the IONP agglomerates remaining after switching off the field will be dissociated as long as the particles will no longer be bridged by CUR molecules after CUR release. A separate study of CUR release is required at in this respect.

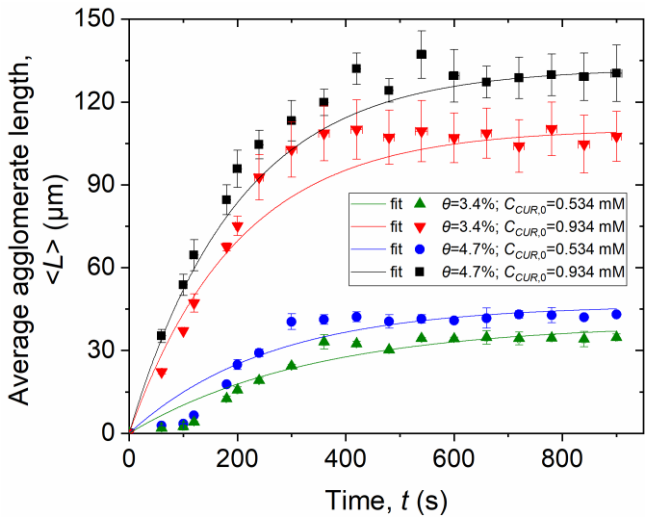

Figure 7. Dependencies of the average length of field-induced agglomerates on the time (elapsed from the switching on the magnetic field) for the βCD-FF-CUR samples at different functionalization degrees θ and different CUR concentrations $C_{CUR,0}$ and fixed magnetic field H=13.5 kA/m.

To quantify the secondary agglomeration, using the snapshots of Figure 6, we measured the distribution of the aggregate length L at different elapsed times from the moment of the magnetic field application. These distributions are shown in Figure S12 for a particular case of $C_{CUR,0}$=0.934 mM and θ=4.7 % mol and exhibit a general tendency of spreading with time, while the distribution peak shifts to larger values of L. The evolution of the average aggregate length $<L>$ with elapsed time is shown in Figure 7 for different values of $C_{CUR,0}$ and θ. In all the cases, the aggregate average length increases with time and reaches a plateau at t>300 s. Qualitatively, Figure 7 correctly reflects all the tendencies shown on the snapshots of Figure 6: progressive increase of the agglomerate size with time; the small difference between the samples at θ=3.4% mol and 4.7% mol at a fixed CUR concentration $C_{CUR,0}$ and the strong difference between the samples at $C_{CUR,0}$=0.534 mM and 0.934 mM at a fixed functionalization degree θ.

For quantitative comparison between different curves, we fit each curve by the following function, whose physical relevance is shown in Appendix: $L(t) = L_{max}(1 - \exp(-t/\tau_a))$ with two adjustable parameters L_{max} (maximal aggregate length at steady state) and τ_a (characteristic time of field-induced agglomeration), whose values are listed in Table S2. The characteristic time lies in the interval between 167 and 300 s for all the samples and is judged to be fast enough for the drug delivery application. The maximum length L_{max} increases by about three times with an increase of the CUR concentration from $C_{CUR,0}$=0.534 mM to 0.934 mM. This qualitatively agrees with the linear increase of the hydrodynamic size of primary agglomerates [Figure S8] leading to stronger magnetic dipolar interactions between them and, consequently, to larger field-induced agglomerates. However, the difference of L_{max} for two functionalization degrees θ=3.4% mol and 4.7% mol is less noticeable, being about only 20%. This correlates with a moderate difference of the hydrodynamic size of the primary agglomerates at θ=3.4% mol and 4.7% mol (cf. Table S1, Figure S8) and with close values of the surface density n_{CUR} of bound CUR that, near the adsorption quasi-plateau, are slightly below the surface density of available βCD, that is n_{max}=0.62 nm^{-2} and 0.77 nm^{-2} for θ=3.4% mol and 4.7% mol, respectively. These trends will be important for understanding the effect of CUR concentration and βCD functionalization degree on the magnetic separation of IONP, which is expected to be strongly enhanced by the primary and secondary IONP agglomeration.

It is worth noticing that the field-induced agglomeration can sometimes be strongly affected by the finite size of the channel. However, in our experiments, the aggregate size is always much smaller than the channel size, and no specific interaction with channel walls was observed. Moreover, in previous studies with similar magnetic colloids, we have found that the channel width does not influence the aggregate size distribution[36,74]. All these arguments allow discarding the confinement effects in the present experimental conditions.

Magnetic separation

Mixtures of βCD-ferrofluids with CUR/ethanol solution (βCD-FF-CUR samples at c_w=8 g/L) were pushed through the microfluidic channel equipped with a magnetizable micropillar in the presence of an external magnetic field of intensity H=13.5kA/m, as described in detail in Subsection "Secondary (field-induced) agglomeration and magnetic separation of IONP" of the Experimental Section. The external uniform magnetic field magnetizes the micropillar and creates strong field gradients around it. To better illustrate the field perturbation around the micropillar, we superposed an image with calculated magnetic field lines to one of the snapshots of Figure 8 showing a naked micropillar. The primary and secondary IONP agglomerates are attracted to the micropillar and are separated from the suspending liquid. The captured IONP form two deposits around the micro-pillar. The full resolution version of Figure 8 is available as a separate .tiff file in SI.

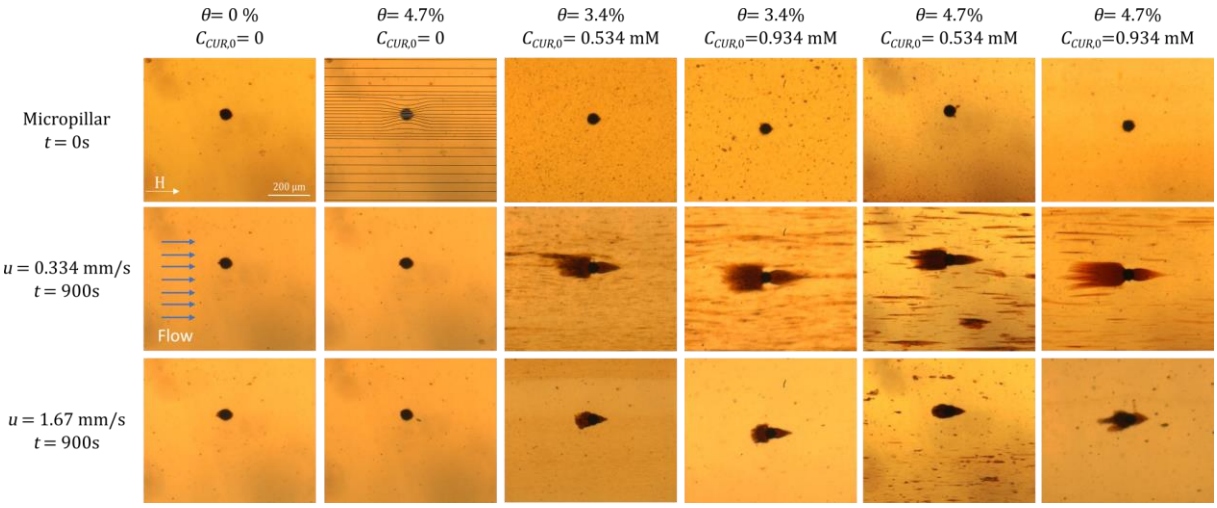

Figure 8. Snapshots of magnetic separation of a βCD-FF-CUR mixture on a magnetizable micropillar under the flow through a microfluidic channel in the presence of an external magnetic field H=13.5 kA/m. The first row shows bare micropillars at t=0, the second and third rows show the capture of IONP by the micropillar at u=0.334 and 1.67 mm/s and elapsed time t=15 min. The first and the second columns show the magnetic separation of bare IONP (acid ferrofluid at pH=2.95) and βCD-coated IONP, respectively, both in the absence of CUR. The arrow labeled "H" in the left top snapshot indicates the direction of the external homogeneous magnetic field, while the magnetic field lines around the magnetized micropillar are shown on the second snapshot of the 1st row.

For the sake of comparison, the first row of snapshots in Figure 8 shows the naked micropillar (without nanoparticle deposits) at the moment t=0 s, i.e. in the absence of magnetic field with a constant flow speed u=0.334 mm/s. The second and the third rows show the capture of nanoparticles by the micropillar at the time t=15min elapsed from the moment of the magnetic field application and at two different flow speeds. As presented in the kinetics study (Figure 6), some dust particles not interfering with the magnetic separation process are observed on the bottom of the channel. We find that nanoparticle deposit size increases with time in the presence of the applied magnetic field. These deposits have an extended longitudinal shape in the direction of the magnetic field

and the flow. There is an asymmetry of the size of two deposits attached to the micropillar. The front deposit (facing the flow) is considerably larger than the backward one likely because of stronger hydrodynamic tensile forces on the surface of the backward deposit eroding the nanoparticles from its surface, as suggested by Ezzaier et al.[21]

For most of the CUR containing samples, we observe long field-induced agglomerates in the liquid phase flowing around the micropillar. These agglomerates are parallel to the magnetic field and are substantially larger for lower flow speed u=0.334 mm/s as compared to a larger speed of u=1.67 mm/s. This difference is essentially due to the fact that the IONP agglomerates travel for a longer time in the magnetic field at a lower flow speed. Quantitatively, the effective length of the circuit (including the connecting tubing) exposed to the applied magnetic field is on the order of 10 cm, so that the residence time of the primary agglomerates in the applied field $t_{res}=V_c/Q$ is about 1200 s for u=0.334 mm/s and 240 s for u=1.67 mm/s, where V_c is the effective volume of the circuit exposed to the magnetic field. According to the kinetic study in Subsection "Secondary (field-induced) agglomeration", the residence time is comparable to the timescale of the secondary agglomeration (τ_a~300 s). We have however to keep in mind that the timescale of the secondary agglomeration in a moving suspension (present Subsection "Magnetic separation") could be different from that in the quiescent suspension (Subsection "Secondary (field-induced) agglomeration"). In any event, the presence of these field-induced agglomerates increases the IONP capture efficiency by the micropillar and therefore the size of the deposit around it, as is seen by comparing the 2nd and the 3rd rows in Figure 8.

To quantify the magnetic separation process, we measured the relative deposit area $s(t)$ (defined in Subsection "Secondary (field-induced) agglomeration and magnetic separation of IONP" of the Experimental Section) at different elapsed times t. We plot in Figure 9 the experimental dependences $s(t)$ for different values of u and θ and different CUR concentrations $C_{CUR,0}$. We have fitted these curves with a function describing the global kinetics of deposit growth around a micro-pillar, as suggested by general filtration theory[75]: $s(t) = s_m(1 - \exp(-t/\tau_s))$, with the two following adjustable parameters: s_m - the maximum relative deposit area, which characterizes the maximal retention capacity of the filtration system, and τ_s - the timescale required for magnetic separation. This equation has been successfully used in our previous studies on magneto-microfluidic separation of different magnetic colloids[21,36]. The values of s_m and τ_s are summarized in Table S3.

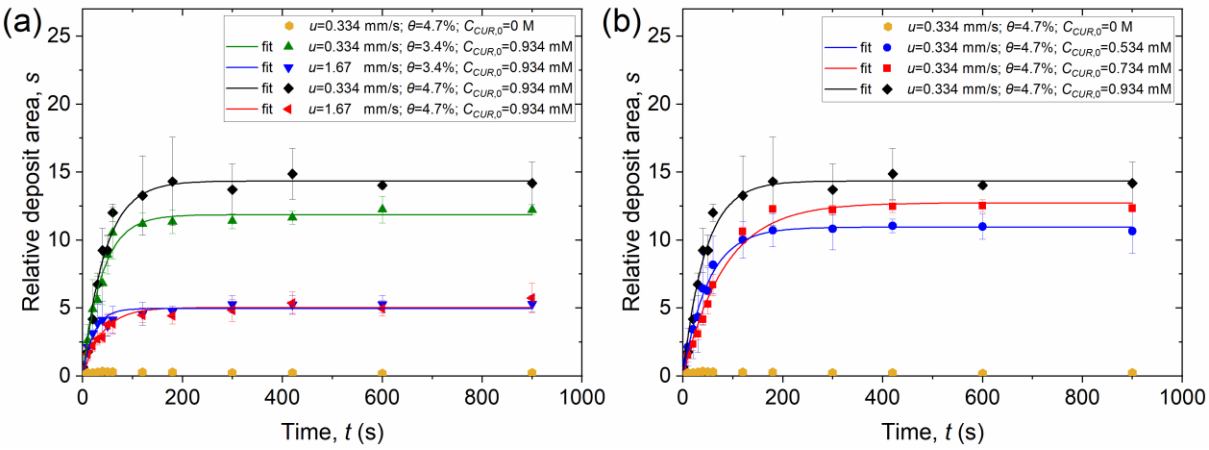

Figure 9. Relative deposit area as a function of elapsed time. Figures (a) and (b) show comparisons for different values of the CUR concentration $C_{CUR,0}$, functionalization degree θ and flow speeds u.

First, one finds only very small nanoparticle deposits around the micropillar in the absence of added CUR (s_m~0.3) in agreement with the snapshots showing negligible capture of both bare IONP (acid ferrofluid at pH=2.95, cf. 1st column of Figure 8) and βCD-coated IONP (2nd column of Figure 8). Weakness of nanoparticle capture from these relatively stable samples correlates with the absence of field-induced agglomeration in the absence of CUR (1st row on Figure 6). This also indicates that non-magnetic interactions between IONP and micropillar are rather weak. On the other hand, relatively large deposits are observed in the presence of CUR (s_m~4 – 15) thanks to the relatively strong attraction of agglomerated IONP to the magnetized micropillar. The experimental $s(t)$ curve for zero CUR is shown by orange hexagons in Figures 9a and b. Second, as already mentioned, the increasing flow speed provokes a decrease in the deposit size (Figure 9a, Table S3). The characteristic time τ_s of magnetic separation decreases roughly in inverse proportion with the flow speed u, following previous theoretical predictions[21].

Let us now focus on the effect of the βCD functionalization degree θ and the CUR molar concentration $C_{CUR,0}$ on the magnetic separation parameters s_m and τ_s. As is seen in Figure 9a and b and Table S3, the functionalization degree θ and the CUR concentration generally increase the maximum deposit size. This increase is substantial when one compares the samples free from CUR with the ones of the minimal CUR concentration used in our experiments (s_m increases from ~0.3 at $C_{CUR,0}$=0 to ~10 at $C_{CUR,0}$=0.534 mM). However, this increase is quite modest above $C_{CUR,0}$=0.534 mM (27% gain between 0.534 and 0.934 mM). The effect of the functionalization degree is also moderate (maximum enhancement of 22% in the range θ=3.4 – 4.7% mol). A surprisingly small effect of both parameters on the steady-state size of the deposits can be explained as follows. According to Magnet et al.[76], the deposit size is defined by the balance of the magnetophoretic and hydrodynamic fluxes of the secondary agglomerates in the vicinity of the deposit surface. The ratio between these fluxes depends only logarithmically on the aggregate length[31] likely leading to a weak dependence of the steady-state deposit size on θ and $C_{CUR,0}$ even at quite different sizes of the primary and secondary agglomerates for different samples. The effect of θ and $C_{CUR,0}$ on the characteristic time τ_s of the magnetic separation is less

clear but globally the timescale fits the interval τ_s~20 – 80 s for the considered range of experimental parameters and is comparable to the timescale of the field-induced agglomeration (τ_a~160 – 300 s) and is believed to be suitable for drug delivery application.

CONCLUSION

This paper is focused on the study of the effect of the curcumin (CUR) binding to β-cyclodextrin (βCD)-coated iron oxide nanoparticles (IONP) on the primary (adsorption-induced) and secondary (field-induced) agglomeration of IONP, as well as on IONP the magnetic separation under flow through a microfluidic channel equipped with a magnetizable micropillar. The main results of this study can be summarized as follows:

(1) The addition of CUR to βCD-ferrofluids leads to CUR binding (adsorption) onto the IONP surface with the maximum surface density of bound CUR being close to the surface density ($n_{\beta CD}$≈0.62 nm^{-2} or 0.77 nm^{-2}) of βCD available on the surface of each individual nanoparticle. Adsorption isotherms accessible through fluorescence measurements show some similarity with the monolayer Langmuir model, except for a slight negative slope at high CUR concentration instead of adsorption plateau. Adsorption is expected to be governed by host-guest hydrophobic interactions between dissolved CUR and βCD immobilized on the IONP surface through the formation of 1:1 and possibly 2:1 βCD:CUR inclusion complexes (Figure 1).

(2) Adsorption of CUR to βCD-coated IONP leads to primary agglomeration of nanoparticles, shown by a linear increase of the hydrodynamic size d_H with the concentration of added CUR, cf. Figure S8. The primary agglomeration is assumed to be caused by the formation of 2:1 βCD:CUR inclusion complexes bridging neighboring IONP (Figure 1). Even though we were unable to explicitly prove the formation of 2:1 inclusion complexes, many factors support this key hypothesis. First, there is a strong correlation between CUR adsorption and agglomeration of βCD-coated IONP, sharing similar kinetics (at a timescale ~20-30 min). Second, a final negative slope of the adsorption isotherms could be related to an increasing number of 2:1 inclusion complexes per agglomerate, leading to an increase in the agglomerate size. Third, no CUR adsorption onto bare IONP (green triangles in Figure S7b) and no change of the hydrodynamic size of bare IONP/CUR mixtures was observed. Finally, the magnetic field-induced agglomerates do not disappear after switching off the field, likely because magnetic dipolar interactions between nanoparticles promote CUR-mediated bridging of neighboring nanoparticles that remain bound to each other when the field is removed.

(3) Increasing size d_H of primary agglomerates with increasing CUR concentration facilitates the formation of the secondary needle-like agglomerates under external magnetic fields and their separation from the flowing suspension on a magnetized micropillar. This is because the energy E_d of the magnetic dipolar interaction between primary agglomerates scales with the cube of their linear size, d_H. The size of the secondary agglomerates and of the IONP deposits around the micropillar follows similar kinetics with comparable timescales (τ_a=160-300 s for field-induced agglomeration and τ_s=20-80 s for magnetic separation). Maximal size of the secondary agglomerates (L_{max}) and IONP deposits (s_m) is an increasing function of CUR concentration $C_{CUR,0}$ and, to a

lesser extent, of the βCD functionalization degree θ. The cause-and-effect relation between these control parameters ($C_{CUR,0}$ and θ) and the efficiency of field-induced agglomeration or magnetic separation can be schematized as follows:

$$\binom{C_{CUR,0}\ \nearrow}{\theta\ \nearrow} \longrightarrow d_H\ \nearrow \longrightarrow E_d\ \nearrow \longrightarrow \binom{L_{max}\ \nearrow}{s_m\ \nearrow},$$

where the "↗" symbol on the right of each physical quantity stands for an increase of the given quantity.

From the practical perspective, we learn that the field-induced agglomeration and magnetic separation of βCD-coated IONP are relatively fast processes (with the longest timescale ~5 min) compatible with *in-vivo* magnetic drug delivery applications. From the general perspective, primary and secondary nanoparticle agglomeration promoted by, respectively, inclusion complexation and magnetic field, are phenomena belonging to the family of stimuli-responsive self-assembly of nanoparticles[77,78].

APPENDIX. EVOLUTION OF THE AVERAGE SIZE OF THE SECONDARY AGGLOMERATES WITH TIME

We have recently shown that in the absence of coalescence, the average volume of the field-induced agglomerates obeys the following evolution equation[36]: $V = V_{max}(1 - \exp(-t/\tau_a))$. The aggregate length-to-diameter ratio is governed by the energy minimum principle and, according to the recent study[74], it gives a linear relationship between the aggregate average volume $<V>$ and the average length $<L>$, within the range of the experimental parameters of the present study. This justifies the evolution law $L = L_{max}(1 - \exp(-t/\tau_a))$ for the secondary agglomerate length used in Subsection "Secondary (field-induced) agglomeration" of Results and Discussion Section.

SUPPORTING INFORMATION

File "Supporting-information-Queiros-Campos-et-al-R1.pdf": Characterization of bare and β-cyclodextrin coated nanoparticles (TEM, VSM, TGA, NMR, conductimetric titration) (Section A); Curcumin binding to β-cyclodextrin coated nanoparticles (fluorescence data, DLS, adsorption isotherms) (Section B); Image processing (Section C); Field-induced agglomeration and magnetic separation (Section D).

File "Fig6.tif": full resolution image of Figure 6.

File "Fig8.tif": full resolution image of Figure 8.

ACKNOWLEDGEMENTS

The authors are very grateful to Drs. Marc Gaysinski and Sophie Pagnota for helping in NMR and TEM measurements, Dr. Cyrille Claudet and Yaroslava Izmailov for microfluidic fabrication, Drs. Claire Lomenech, Charlotte Hurel and Jéssica A. Marins for the help in chemical analyses, Dr. Hélène Guizouarn for the use of the plate reader, as well as Prof. Gian Luca Lippi for helpful discussions. PK and GG acknowledge the French 'Agence Nationale de la Recherche', Project Future Investments UCA JEDI, No. ANR-15-IDEX-01 (projects ImmunoMag and MagFilter) and the private company Axlepios Biomedical for financial support; JQC acknowledges the financial support of UCA JEDI and Axlepios Biomedical through the PhD fellowship. JMGF acknowledges financial support from

Ministerio de Ciencia, Innovación y Universidades, Agencia Estatal de Investigación and the European Regional Development Funds (FEDER-UE) (project RTI2018-097609-B-C21), and from Junta de Andalucía (project P20_0016).

REFERENCES

(1) Pankhurst, Q. A., Connolly, J., Jones, S. K., & Dobson, J. (2003). Applications of magnetic nanoparticles in biomedicine. Journal of physics D: Applied physics, 36(13), R167.
(2) Tran, N., & Webster, T. J. (2010). Magnetic nanoparticles: biomedical applications and challenges. Journal of Materials Chemistry, 20(40), 8760-8767.
(3) Costo, R., Bello, V., Robic, C., Port, M., Marco, J. F., Puerto Morales, M., & Veintemillas-Verdaguer, S. (2012). Ultrasmall iron oxide nanoparticles for biomedical applications: improving the colloidal and magnetic properties. Langmuir, 28(1), 178-185.
(4) Manna, P. K., Nickel, R., Wroczynskyj, Y., Yathindranath, V., Li, J., Liu, S., Thliveris, J.A.; Klonisch, T.; Miller, D.W; & van Lierop, J. (2018). Simple, hackable, size-selective, amine-functionalized Fe-oxide nanoparticles for biomedical applications. Langmuir, 34(8), 2748-2757.
(5) Ferretti, A. M., Usseglio, S., Mondini, S., Drago, C., La Mattina, R., Chini, B., Verderio C., Leonzino M., Cagnoli C., Joshi P., Boraschi D., Italiani P., Li Y., Swartzwelter B.J., Sironi L., Gelosa P., Castiglioni L., Guerrini U. & Ponti, A. (2021). Towards bio-compatible magnetic nanoparticles: Immune-related effects, in-vitro internalization, and in-vivo bio-distribution of zwitterionic ferrite nanoparticles with unexpected renal clearance. Journal of Colloid and Interface Science, 582, 678-700.
(6) Yavuz, C. T., Prakash, A., Mayo, J. T., & Colvin, V. L. (2009). Magnetic separations: from steel plants to biotechnology. Chemical Engineering Science, 64(10), 2510-2521.
(7) Ambashta, R. D., & Sillanpää, M. (2010). Water purification using magnetic assistance: a review. Journal of hazardous materials, 180(1-3), 38-49
(8) Mudassir, M. A., Hussain, S. Z., Jilani, A., Zhang, H., Ansari, T. M., & Hussain, I. (2019). magnetic hierarchically macroporous emulsion-templated poly (acrylic acid)–iron oxide nanocomposite beads for water Remediation. Langmuir, 35(27), 8996-9003.
(9) Biehl, P., Wiemuth, P., Lopez, J. G., Barth, M. C., Weidner, A., Dutz, S., Peneva, K.; & Schacher, F. H. (2020). Weak Polyampholytes at the Interface of Magnetic Nanocarriers: A Facile Catch-and-Release Platform for Dyes. Langmuir, 36(22), 6095-6105.
(10) Douziech-Eyrolles, L.; Marchais, H.; Herve, K.; Munnier, E.; Souce, M.; Linassier, C.; Dubois, P.; Chourpa, I. Nanovectors for anticancer agents based on superparamagnetic iron oxide nanoparticles. Int. J. Nanomed. 2007, 2, 541–550
(11) Estelrich, J., Escribano, E., Queralt, J., & Busquets, M. A. (2015). Iron oxide nanoparticles for magnetically-guided and magnetically-responsive drug delivery. International journal of molecular sciences, 16(4), 8070-8101.
(12) Momtazi, L., Bagherifam, S., Singh, G., Hofgaard, A., Hakkarainen, M., Glomm, W. R., Roos N. Mælandsmo G.M., Griffiths G. & Nyström, B. (2014). Synthesis, characterization, and cellular uptake of magnetic nanocarriers for cancer drug delivery. Journal of colloid and interface science, 433, 76-85.
(13) Dałek, P., Borowik, T., Reczyńska, K., Pamuła, E., Chrzanowski, W., & Langner, M. (2020). Evaluation of the In Vitro Stability of Stimuli-Sensitive Fatty Acid-Based Microparticles for the Treatment of Lung Cancer. Langmuir, 36(37), 11138-11146.
(14) Blums, E., Cebers, A., and Mayorov, M. M., Magnetic Fluids; Walter de Gruyters, Berlin: Germany, 1997.
(15) Schwaminger, S. P., Fraga-García, P., Blank-Shim, S. A., Straub, T., Haslbeck, M., Muraca, F., Dawson, K.A. & Berensmeier, S. (2019). Magnetic one-step purification of his-tagged protein by bare iron oxide nanoparticles. ACS omega, 4(2), 3790-3799.
(16) Gijs, M. A., Lacharme, F., & Lehmann, U. (2010). Microfluidic applications of magnetic particles for biological analysis and catalysis. Chemical reviews, 110(3), 1518-1563.
(17) Song, D., Yang, R., Long, F., & Zhu, A. (2019). Applications of magnetic nanoparticles in surface-enhanced Raman scattering (SERS) detection of environmental pollutants. Journal of Environmental Sciences, 80, 14-34.
(18) Mandel, K., & Hutter, F. (2012). The magnetic nanoparticle separation problem. Nano Today, 7(6), 485-487.

(19) Leong, S. S., Ahmad, Z., Low, S. C., Camacho, J., Faraudo, J., & Lim, J. (2020). Unified view of magnetic nanoparticle separation under magnetophoresis. Langmuir, 36(28), 8033-8055.
(20) Moeser, G. D., Roach, K. A., Green, W. H., Alan Hatton, T., & Laibinis, P. E. (2004). High-gradient magnetic separation of coated magnetic nanoparticles. AIChE Journal, 50(11), 2835-2848.
(21) Ezzaier, H., Marins, J. A., Claudet, C., Hemery, G., Sandre, O., & Kuzhir, P. (2018). Kinetics of aggregation and magnetic separation of multicore iron oxide nanoparticles: effect of the grafted layer thickness. Nanomaterials, 8(8), 623.
(22) Eberbeck, D., Kettering, M., Bergemann, C., Zirpel, P., Hilger, I., & Trahms, L. (2010). Quantification of the aggregation of magnetic nanoparticles with different polymeric coatings in cell culture medium. Journal of Physics D: Applied Physics, 43(40), 405002
(23) Liu, S., Han, Y., Qiao, R., Zeng, J., Jia, Q., Wang, Y., & Gao, M. (2010). Investigations on the interactions between plasma proteins and magnetic iron oxide nanoparticles with different surface modifications. The Journal of Physical Chemistry C, 114(49), 21270-21276.
(24) Lartigue, L., Wilhelm, C., Servais, J., Factor, C., Dencausse, A., Bacri, J. C., Luciani, N.; & Gazeau, F. (2012). Nanomagnetic sensing of blood plasma protein interactions with iron oxide nanoparticles: impact on macrophage uptake. Acs Nano, 6(3), 2665-2678.
(25) Wiogo, H. T., Lim, M., Bulmus, V., Gutiérrez, L., Woodward, R. C., & Amal, R. (2012). Insight into serum protein interactions with functionalized magnetic nanoparticles in biological media. Langmuir, 28(9), 4346-4356.
(26) Etheridge, M. L., Hurley, K. R., Zhang, J., Jeon, S., Ring, H. L., Hogan, C., Haynes, Ch. L.; Garwood, M.; & Bischof, J. C. (2014). Accounting for biological aggregation in heating and imaging of magnetic nanoparticles. Technology, 2(03), 214-228.
(27) Guibert, C., Dupuis, V., Peyre, V., & Fresnais, J. (2015). Hyperthermia of magnetic nanoparticles: experimental study of the role of aggregation. The Journal of Physical Chemistry C, 119(50), 28148-28154.
(28) Cabrera, D., Camarero, J., Ortega, D., & Teran, F. J. (2015). Influence of the aggregation, concentration, and viscosity on the nanomagnetism of iron oxide nanoparticle colloids for magnetic hyperthermia. Journal of Nanoparticle Research, 17(3), 121.
(29) Pilati, V., Gomide, G., Gomes, R. C., Goya, G. F., & Depeyrot, J. (2021). Colloidal Stability and Concentration Effects on Nanoparticle Heat Delivery for Magnetic Fluid Hyperthermia. Langmuir, 37(3), 1129-1140.
(30) Talbot, D., Queiros Campos, J., Checa-Fernandez Blanca L., A. Marins J., Lomenech, C., Hurel, C., D. Godeau, G., Raboisson-Michel M., Verger-Dubois, G., Obeid, L., Kuzhir, P. and Bee A. Adsorption of Organic Dyes on Magnetic Iron Oxide Nanoparticles. Part I: Mechanisms and Adsorption-Induced Nanoparticle Agglomeration . *ACS Omega* 2021, 6, 19086−19098.
(31) Ezzaier, H., Alves Marins, J., Razvin, I., Abbas, M., Ben Haj Amara, A., Zubarev, A., & Kuzhir, P. (2017). Two-stage kinetics of field-induced aggregation of medium-sized magnetic nanoparticles. The Journal of chemical physics, 146(11), 114902.
(32) Mohapatra, D. K; Philip, J. Effect of surface charge screening on critical magnetic fields during field induced structural transitions in magnetic fluids. J. Appl. Phys. 2019, 125, 244301.
(33) Yeap, S. P., Ahmad, A. L., Ooi, B. S., & Lim, J. (2012). Electrosteric stabilization and its role in cooperative magnetophoresis of colloidal magnetic nanoparticles. Langmuir, 28(42), 14878-14891.
(34) Tham, F. K., Ng, W. M., Leong, S. S., Yeap, S. P., Low, S. C., Lee, H. L., & Lim, J. (2021). Magnetophoresis of Magnetic Pickering Emulsions Under Low Field Gradient: Macroscopic and Microscopic Motion. Langmuir, 37(5), 1811-1822.
(35) Kuzhir, P., Magnet, C., Ezzaier, H., Zubarev, A., & Bossis, G. (2017). Magnetic filtration of phase separating ferrofluids: From basic concepts to microfluidic device. Journal of Magnetism and Magnetic Materials, 431, 84-90.
(36) Queiros Campos J., B.L. Checa-Fernandez, J. A. Marins, C. Lomenech, Ch. Hurel, G.Godeau, M. Raboisson-Michel, G. Verger-Dubois, A. Bee, D. Talbot, and P. Kuzhir. Adsorption of organic dyes on magnetic iron oxide nanoparticles. Part II: Field-induced nanoparticle agglomeration and magnetic separation. *Langmuir* 2021,37, 10612-10623.
(37) Sharma, R. A., Gescher, A. J., & Steward, W. P. (2005). Curcumin: the story so far. European journal of cancer, 41(13), 1955-1968.

(38) Manju, S., & Sreenivasan, K. (2011). Enhanced drug loading on magnetic nanoparticles by layer-by-layer assembly using drug conjugates: blood compatibility evaluation and targeted drug delivery in cancer cells. Langmuir, 27(23), 14489-14496.
(39) Bhandari, R., Gupta, P., Dziubla, T., & Hilt, J. Z. (2016). Single step synthesis, characterization and applications of curcumin functionalized iron oxide magnetic nanoparticles. Materials Science and Engineering: C, 67, 59-64.
(40) Justin, C., Samrot, A. V., Sahithya, C. S., Bhavya, K. S., & Saipriya, C. (2018). Preparation, characterization and utilization of coreshell super paramagnetic iron oxide nanoparticles for curcumin delivery. PLoS One, 13(7), e0200440.
(41) Pourjavadi, A., Asgari, S., Hosseini, S. H., & Akhlaghi, M. (2018). Codelivery of hydrophobic and hydrophilic drugs by graphene-decorated magnetic dendrimers. Langmuir, 34(50), 15304-15318.
(42) Khan, S., Setua, S., Kumari, S., Dan, N., Massey, A., Hafeez, B. B., Yallapu, M.M., Stiles Z. E., Alabkaa A., Yue J., Ganju A., Behrman S., Jaggi, M. & Chauhan, S. C. (2019). Superparamagnetic iron oxide nanoparticles of curcumin enhance gemcitabine therapeutic response in pancreatic cancer. Biomaterials, 208, 83-97.
(43) Elbialy, N.S., Abdelfatah, E.A. & Khalil, W.A. Antitumor Activity of Curcumin-Green Synthesized Gold Nanoparticles: In Vitro Study. *BioNanoSci.* **9,** 813–820 (2019).
(44) Gholibegloo, E., Mortezazadeh, T., Salehian, F., Forootanfar, H., Firoozpour, L., Foroumadi, A., Ramazani A. & Khoobi, M. (2019). Folic acid decorated magnetic nanosponge: An efficient nanosystem for targeted curcumin delivery and magnetic resonance imaging. Journal of colloid and interface science, 556, 128-139.
(45) Jayaprabha, K. N., & Joy, P. A. (2015). Citrate modified β-cyclodextrin functionalized magnetite nanoparticles: a biocompatible platform for hydrophobic drug delivery. RSC Advances, 5(28), 22117-22125.
(46) Rajbanshi, B., Saha, S., Das, K., Barman, B. K., Sengupta, S., Bhattacharjee, A., & Roy, M. N. (2018). Study to probe subsistence of host-guest inclusion complexes of α and β-cyclodextrins with biologically potent drugs for safety regulatory dischargement. Scientific reports, 8(1), 1-20.
(47) Viglianti, C., Hanna, K., De Brauer, C., & Germain, P. (2006). Removal of polycyclic aromatic hydrocarbons from aged-contaminated soil using cyclodextrins: experimental study. Environmental Pollution, 140(3), 427-435.
(48) Petitgirard, A., Djehiche, M., Persello, J., Fievet, P., Fatin-Rouge, N., 2009. PAH contaminated soil remediation by reusing an aqueous solution of cyclodextrins. Chemosphere 75, 714–718.
(49) Liu, H., Cai, X., Wang, Y., & Chen, J. (2011). Adsorption mechanism-based screening of cyclodextrin polymers for adsorption and separation of pesticides from water. Water research, 45(11), 3499-3511.
(50) Zhang, D., Hao, R., Zhang, L., You, H., & Fang, J. (2020). Ratiometric sensing of polycyclic aromatic hydrocarbons using capturing ligand functionalized mesoporous au nanoparticles as a surface-enhanced raman scattering substrate. Langmuir, 36(38), 11366-11373.
(51) Law, H., Benito, J. M., Garcia Fernandez, J. M., Jicsinszky, L., Crouzy, S., & Defaye, J. (2011). Copper (II)-complex directed regioselective mono-p-toluenesulfonylation of cyclomaltoheptaose at a primary hydroxyl group position: an NMR and molecular dynamics-aided design. The Journal of Physical Chemistry B, 115(23), 7524-7532.
(52) Petter, R. C., Salek, J. S., Sikorski, C. T., Kumaravel, G., & Lin, F. T. (1990). Cooperative binding by aggregated mono-6-(alkylamino)-. beta.-cyclodextrins. Journal of the American Chemical Society, 112(10), 3860-3868.
(53) Massart, R. (1981). Preparation of aqueous magnetic liquids in alkaline and acidic media. IEEE transactions on magnetics, 17(2), 1247-1248.
(54) Tornøe, C. W., Christensen, C., & Meldal, M. (2002). Peptidotriazoles on solid phase:[1, 2, 3]-triazoles by regiospecific copper (I)-catalyzed 1, 3-dipolar cycloadditions of terminal alkynes to azides. The Journal of organic chemistry, 67(9), 3057-3064.
(55) Rostovtsev, V. V., Green, L. G., Fokin, V. V., & Sharpless, K. B. (2002). A stepwise huisgen cycloaddition process: copper (I)-catalyzed regioselective "ligation" of azides and terminal alkynes. Angewandte Chemie, 114(14), 2708-2711.
(56) Sehgal, A., Lalatonne, Y., Berret, J. F., & Morvan, M. (2005). Precipitation— redispersion of cerium oxide nanoparticles with poly (acrylic acid): toward stable dispersions. Langmuir, 21(20), 9359-9364
(57) Rosensweig, R. E. Ferrohydrodynamics; Cambridge University Press, Cambridge:UK, 1985.

(58) Cabuil, V.; Perzynski, R. Particle size determination in magnetic fluids. In Magnetic Fluids and Handbook Applications; Berkovski, V.; Bashtovoi, V., Eds.; Begell house: New York and Wallinford (UK), 1996
(59) Miller, N. P.; Berg, J. C.; O'Brien, R. W. The electrophoretic mobility of a porous aggregate. J. Colloid Interface Sci. 1992, 153, 237-243
(60) Ezzaier, H. Aggregation and magnetic separation of magnetic nanoclusters. Doctoral dissertation, University of Nice-Sophia Antipolis, 2017 (in French).
(61) Palepu, R., Richardson, J. E., & Reinsborough, V. C. (1989). Binding constants of. beta.-cyclodextrin/surfactant Inclusion by conductivity measurements. Langmuir, 5(1), 218-221.
(62) Shen, Yingzhuo, Ali Farajtabar, Jie Xu, Jiali Wang, Yuanyuan Xia, Hongkun Zhao, et Renjie Xu. (avril 2019) Thermodynamic Solubility Modeling, Solvent Effect and Preferential Solvation of Curcumin in Aqueous Co-Solvent Mixtures of Ethanol, n-Propanol, Isopropanol and Propylene Glycol . *The Journal of Chemical Thermodynamics* 131, 410‑419
(63) Morales, M. P., Serna, C. J., Bødker, F., & Mørup, S. (1997). Spin canting due to structural disorder in maghemite. Journal of Physics: Condensed Matter, 9(25), 5461
(64) Russel, W. B., Saville, D. A., & Schowalter, W. R. Colloidal dispersions. Cambridge university press, Cambridge: UK, 1991.
(65) Chibowski, S., & Wiśniewska, M. (2002). Study of electrokinetic properties and structure of adsorbed layers of polyacrylic acid and polyacrylamide at Fe2O3–polymer solution interface. Colloids and Surfaces A: Physicochemical and Engineering Aspects, 208(1-3), 131-145.
(66) Hajdú, A., Szekeres, M., Tóth, I. Y., Bauer, R. A., Mihály, J., Zupkó, I., & Tombácz, E. (2012). Enhanced stability of polyacrylate-coated magnetite nanoparticles in biorelevant media. Colloids and Surfaces B: Biointerfaces, 94, 242-249.
(67) Marins, J. A., Montagnon, T., Ezzaier, H., Hurel, C., Sandre, O., Baltrunas, D., Mazeika K., Petrov A. & Kuzhir, P. (2018). Colloidal stability of aqueous suspensions of polymer-coated iron oxide nanorods: implications for biomedical applications. ACS Applied Nano Materials, 1(12), 6760-6772.
(68) Tønnesen, H. H., & Karlsen, J. (1985). Studies on curcumin and curcuminoids. Zeitschrift für Lebensmittel-Untersuchung und Forschung, 180(5), 402-404.
(69) Wang, Z., Leung, M. H., Kee, T. W., & English, D. S. (2010). The role of charge in the surfactant-assisted stabilization of the natural product curcumin. Langmuir, 26(8), 5520-5526
(70) Baglole K. N., Boland P. G. and Wagner B. D., 2005, « Fluorescence enhancement of curcumin upon inclusion into parent and modified cyclodextrins », *Journal of Photochemistry and Photobiology A: Chemistry*, 2005, 173, 230-237.
(71) Hill, T. L. An introduction to statistical thermodynamics. Dover Publications Inc.: New York, 1986
(72) Daynès, A., Temurok, N., Gineys, J. P., Cauet, G., Nerin, P., Baudry, J., & Bibette, J. (2015). Fast magnetic field-enhanced linear colloidal agglutination immunoassay. Analytical chemistry, 87(15), 7583-7587.
(73) Stella, V. J., Rao, V. M., Zannou, E. A., & Zia, V. (1999). Mechanisms of drug release from cyclodextrin complexes. Advanced drug delivery reviews, 36(1), 3-16.
(74) Raboisson-Michel, M., Queiros Campos, J., Schaub, S., Zubarev, A., Verger-Dubois, G., & Kuzhir, P. (2020). Kinetics of field-induced phase separation of a magnetic colloid under rotating magnetic fields. The Journal of Chemical Physics, 153(15), 154902.
(75) Tien, C.; Ramarao, B.V. Granular Filtration of Aerosols and Hydrosols; Elsevier Science & Technology Books: New York, NY: USA, 2007.
(76) Magnet, C., Kuzhir, P., Bossis, G., Meunier, A., Nave, S., Zubarev, A., C. Lomenech & Bashtovoi, V. (2014). Behavior of nanoparticle clouds around a magnetized microsphere under magnetic and flow fields. Physical Review E, 89(3), 032310.
(77) Grzelczak, M., Liz-Marzán, L. M., & Klajn, R. (2019). Stimuli-responsive self-assembly of nanoparticles. Chemical Society Reviews, 48(5), 1342-1361.
(78) Hwang, E. Y., Lee, J. S., & Lim, D. W. (2019). Oppositely Charged, Stimuli-Responsive Anisotropic Nanoparticles for Colloidal Self-Assembly. Langmuir, 35(13), 4589-4602.

Table of content Graphic (TOC)